nature geoscience

Article

https://doi.org/10.1038/s41561-025-01847-5

Major terrestrial contribution to the dissolved organic carbon budget in the Arctic Ocean

Received: 9 January 2025

Accepted: 7 October 2025

Published online: 07 November 2025

Check for updates

Xianyu Kong[1], Oliver J. Lechtenfeld[2], Jan M. Kaesler[2], Mats A. Granskog[3], Colin A. Stedmon[4], Martin Graeve[1] & Boris P. Koch[1,5]

Arctic warming is expected to increase the terrestrial dissolved organic carbon flux into the central Arctic Ocean, altering biogeochemical cycling by modulating light attenuation, microbial respiration and carbon dioxide release. Quantifying terrestrial inputs remains challenging due to biases in common proxies and uncertainties in endmember characteristics, which complicate traditional mixing models, introducing uncertainties in predicting climate change impacts. Here we present a high-resolution mass spectrometric approach allowing direct analysis of original seawater, tracing and quantifying terrestrial contributions to dissolved organic carbon. Terrestrial dissolved organic carbon in the central Arctic Ocean contributed at least 0.97 ± 0.05 PgC (16.4%) to the dissolved organic carbon inventory of 5.93 ± 0.09 PgC, including 15.0% in deep water (7.9 ± 0.4 µmol l^{-1}). In surface water within the Transpolar Drift, the average terrestrial dissolved organic carbon concentrations were 117% higher (31.5 ± 4.8 µmol l^{-1}) than outside the Transpolar Drift (14.5 ± 1.0 µmol l^{-1}). The terrestrial dissolved organic matter is compositionally distinct, being more aromatic, hydrophobic and nitrogen-poor than marine sources. This approach provides chemical information that reflects changes in organic matter sources and bioavailability, both of which are central to understanding future climatic impacts on Arctic biogeochemical cycles.

The Arctic Ocean is undergoing drastic changes. Rising temperature alters marine food webs[1], changes terrestrial inputs[2], reduces the extent of sea ice and increases the irradiation of the surface ocean[3]. Dissolved organic matter (DOM) constitutes a large reservoir of organic carbon in the ocean, rivalling the atmospheric CO_2 content in scale[2]. DOM is produced in surface water and sea ice, and acts as a sink for autotrophic carbon and as a source of energy for heterotrophic prokaryotes[4]. Compared with most other oceans, the Arctic Ocean receives more freshwater and a disproportionally large amount of terrestrial DOM (tDOM). The Transpolar Drift (TPD; Fig. 1) is the primary surface current transporting shelf surface waters and sea ice from the Laptev and East Siberian Seas into the central Arctic Ocean (CAO; Fig. 1)[5,6]. Arctic Ocean waters contribute to the Atlantic Meridional Overturning Circulation and to long-term storage of dissolved organic carbon (DOC) in Atlantic deep waters[7,8].

DOM production, transport, removal and accumulation are affected by its concentration and composition, both of which are tightly linked to its sources[4]. Investigating the composition and budget of tDOM is critical for understanding its fate from high latitudes and its integration into the global carbon cycle. As Arctic warming accelerates,

[1]Alfred-Wegener-Institut Helmholtz-Zentrum für Polar- und Meeresforschung, Bremerhaven, Germany. [2]Helmholtz Centre for Environmental Research - UFZ, Leipzig, Germany. [3]Norwegian Polar Institute, Fram Centre, Tromsø, Norway. [4]National Institute of Aquatic Resources, Technical University of Denmark, Kongens Lyngby, Denmark. [5]University of Applied Sciences, Bremerhaven, Germany. e-mail: Xianyu.Kong@awi.de; Boris.Koch@awi.de

https://doi.org/10.1038/s41561-025-01847-5

increasing permafrost thaw, river discharge and coastal erosion are expected to increase the terrestrial DOC (tDOC) stock, altering Arctic biogeochemistry by modulating marine food webs[9], light attenuation[10], microbial respiration[11] and CO_2 release[12]. Identifying the tDOM and associated chemical properties is vital to understand its role in biogeochemistry. Moreover, constraining the tDOM budget is important for improving Earth system model projections[13].

Molecular-level analysis is a promising way of gaining insights into DOM sources and turnover processes. However, the instrumental analysis of DOM in the ocean is challenging because of its extreme chemical complexity, low concentration and the presence of salt. Matrix effects during desalting, chemical fractionation by solid-phase extraction[14], lack of adequate standards and selective ionization of molecules in mass spectrometry[15] hamper quantitative chemical analysis. A more specific approach is ultrahigh-resolution Fourier transform ion cyclotron resonance (FT-ICR) mass spectrometry (MS), which resolves the molecular formula (MF) diversity of DOM[16]. Hyphenation to liquid chromatography (LC) additionally offers advances by further separating DOM according to size or polarity[17]. However, because most mass spectrometric approaches so far depend on solid-phase extraction, matrix effects limit quantification[14]. In an attempt to circumnavigate this, we recently demonstrated that filtered seawater can be analysed at native DOC concentrations by combining LC and FT-ICR-MS (LC–FTMS)[18].

Despite analytical advances, accurately quantifying and characterizing DOM sources remains challenging. Lignin phenols, produced exclusively by vascular plants, serve as an organic tracer for terrestrial plant material, but represent only a subfraction of tDOM and can be selectively removed in the marine environment[19]. The stable carbon isotope ratio ($\delta^{13}C$) has been widely used as a tDOM proxy[20] but is affected by oxidation processes[21] or may be biased when measured from solid-phase extracted DOM[14]. Optical methods (that is, chromophoric DOM and fluorescent DOM (FDOM)) can be used to characterize and quantify DOM, but capture only a subset of the DOM pool[22]. Although tDOM has an intense FDOM signal, a similar signature can also be produced by marine sources, but it results in intensities that are orders of magnitude lower[22]. These factors, combined with uncertainties in endmember characteristics, can complicate the tracing of the fate of tDOM with mixing models. However, strong correlations do exist among salinity, lignin phenols, $\delta^{13}C$ and blue wavelength FDOM signatures (humic-like) observed in the Arctic[23–25], and suggest that covariation patterns among proxies transcend their individual biases. Rather than relying solely on absolute values, leveraging these persistent correlations provides an alternative approach to characterize tDOM.

This study correlates terrestrial proxies and MFs identified by LC–FTMS to distinguish terrestrial, marine and sea ice DOM based on a full-year CAO dataset during the Arctic drift expedition MOSAiC[26] (Multidisciplinary drifting Observatory for the Study of Arctic Climate; Fig. 1). Applying this approach, the study quantifies and characterizes tDOM, and reveals the key environmental factors driving tDOM composition. It provides a depth-resolved estimate of the tDOC inventory in the CAO, and evaluates its role in Arctic carbon cycling.

A mass spectrometric approach to quantify DOM fractions

In our LC–FTMS approach, each analysis of 100 µl seawater yielded an average of 12,475 ± 2,698 (mean ± s.d.) MFs and their respective peak magnitudes for ten retention time segments (representing decreasing polarity). First, we summed peak magnitudes of identical MFs across retention time segments, resulting in an average of 4,574 ± 777 MFs for each sample. The summed magnitudes of all peaks that were assigned with a MF (total assigned intensity; TAI) correlated significantly with DOC concentration ($R^2 = 0.78$; Fig. 2a,c) and integrated fluorescence intensity ($FDOM_{sum}$, $R^2 = 0.72$; Fig. 2b,d), independent of sample region or type, confirming previous results[18]. The terrestrial humic-like fluorescent component with maximum emission at 475 nm

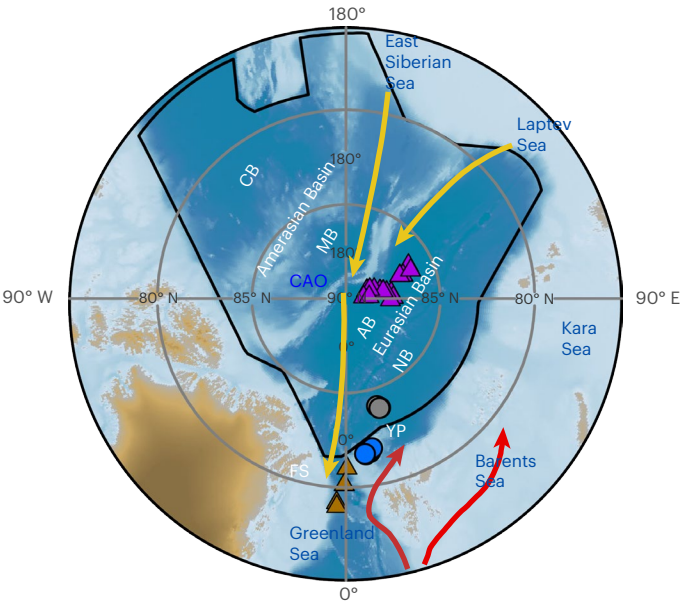

Fig. 1 | Study area of the MOSAiC expedition. The black line in the map represents the boundary of the CAO large marine ecosystem as defined by the Arctic Council[6]. The CAO consists of two major deep basins, the Amerasian Basin with the Canada Basin (CB) and the Makarov Basin (MB), and the Eurasian Basin that comprises the Amundsen Basin (AB) and the Nansen Basin (NB). Yellow arrows indicate the approximate location of the TPD, which varies with the Arctic Oscillation[51]. Red arrows indicate the warm inflow of Atlantic water into the Arctic Ocean. Symbols represent sampling stations in different regions: triangles denote stations within the influence of the TPD (Amundsen Basin (violet triangles) and the western Fram Strait (FS, brown triangles)); circles represent stations outside the TPD (western Nansen Basin (grey circles) and Yermak Plateau (YP, blue circles)). Map generated with ArcGIS Pro 3.3 with GEBCO 2024 bathymetry data from ref. 52.

(C475; Extended Data Fig. 1), identified by parallel factor analysis[27], is prevalent in DOM from large Arctic rivers[28]. Horizontal off-shelf export of FDOM from the Chukchi Sea to the CAO via the TPD has been observed[29], and additional FDOM can originate from Arctic sediments and subsea permafrost[30]. The tDOC quantification applied here was based on the rank of the C475 proxy for the identification of terrestrial MFs (tMFs), followed by quantification based on the strong DOC–TAI calibration: MFs that showed significant positive correlation (Spearman's rank $P < 0.01$) of their mass peak magnitude with C475 were labelled as tMFs ($n = 1,457$) and contributed 16.9–39.9% to the summed magnitudes of all MFs. Of the 40 MFs previously identified as terrestrial markers[31], 37 were also identified as tMFs in our study. Those MFs that were anti-correlated or uncorrelated with C475 were categorized as marine MFs (mMFs). Assuming that the mean ionization efficiency of the tMFs was comparable to the overall mean ionization efficiency, the tDOC and marine DOC (mDOC) fractions in a sample can be calculated. The propagated uncertainty in tDOC concentrations was estimated at ±18.2%, incorporating uncertainties from the DOC measurements, TAI measurements, their correlation and the percentage subfraction assigned to tDOC (Methods). We independently validated the C475-based identification of tMFs by using $\delta^{13}C$ and practical salinity (S_p), yielding an average difference in estimated tDOC concentrations of only −3.5% and +1.1%, respectively (Supplementary Text 2). Additionally, C475 and tDOC correlated significantly with $\delta^{13}C$, S_p and terrestrial index (I_{Terr})[31] (Pearson's $P < 0.001$; Extended Data Fig. 2), supporting the use of C475 as a terrestrial proxy for the identification of tMFs, despite the fact that non-fluorescent tDOC exists. However, as shown above, this approach is flexible and can build on other proxies such at $\delta^{13}C$, as long as they reliably capture Arctic terrestrial gradients.

https://doi.org/10.1038/s41561-025-01847-5

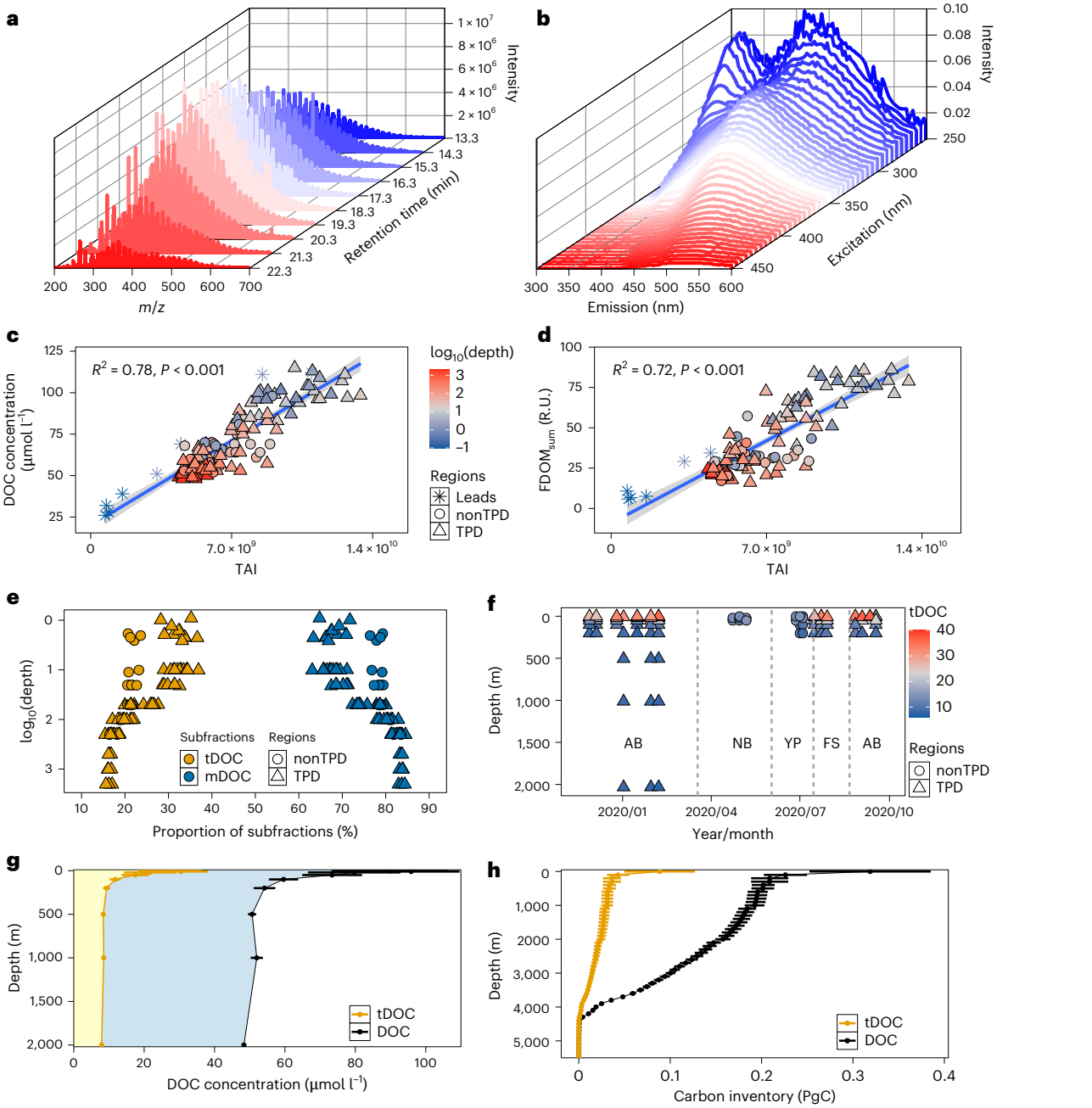

Fig. 2 | Quantification of tDOC in the CAO. a,**b**, Mass spectra of all assigned MFs at different retention times (colours; **a**) and EEMs of FDOM (colours denote excitation wavelengths; **b**) for a surface sample in the Amundsen Basin. **c**,**d**, The summed intensity of all assigned MFs (TAI) correlated with DOC concentration (**c**; $n = 118$; two-sided Pearson correlation, $P < 0.001$) and $FDOM_{sum}$ (integrated intensity from EEMs) for ocean and lead samples (**d**; $n = 105$; two-sided Pearson correlation, $P < 0.001$; symbols and colours as in **c**). Sample groups: surface lead water samples in the Amundsen Basin (asterisks), samples inside the TPD (that is, Amundsen Basin (AB) and western Fram Strait (FS); triangles) and outside the TPD (nonTPD; that is, western Nansen Basin (NB) and Yermak Plateau (YP); circles). Colours represent $\log_{10}$-transformed water depth in metres ($\log_{10}$(depth)). The blue line indicates the linear Pearson regression for all samples. The grey shading represents the 95% confidence interval. R.U., Raman units. **e**, Relative proportion of tDOC (orange circles) and mDOC (blue circles) in the water column ($n = 93$). **f**, Water column distribution of tDOC concentration (μmol l^{-1}) over the time of the MOSAiC expedition ($n = 93$, symbols as in **c**). **g**, Mean tDOC and DOC (±s.d.) concentrations in the water column ($n = 93$; tDOC, light yellow area; mDOC, light blue area). **h**, Depth-integrated tDOC and DOC inventories in 100 m depth intervals (Data are presented as mean ± s.d., $n = 313$; Methods). Note that the carbon inventories at the deepest depths are close to zero because the CAO volume at depths >4,000 m is small.

The tDOC concentration decreased with depth (Fig. 2f,g). In polar surface water, the average tDOC was 25.7 ± 9.0 μmol l^{-1} (28.5 ± 5.4% of total DOC), slightly exceeding a previous isotope-based estimate of 14–24% surface tDOC[24]. Within the TPD surface, average tDOC was 31.5 ± 4.8 μmol l^{-1}, which is 117% higher than outside the TPD (14.5 ± 1.0 μmol l^{-1}) and consistent with significant terrestrial input from Siberian shelves into the Amundsen Basin and western Fram Strait[32]. In deep water, average tDOC was 7.9 ± 0.4 μmol l^{-1} (16.3 ± 0.7% of total DOC), about half of the contribution found in the deep Canada Basin (30%)[33], but five times higher than reported in another study for ultrafiltered tDOC in the deep water of the entire Arctic (~3%)[24]. Both studies are based on δ^{13}C-based mixing models, which may have

https://doi.org/10.1038/s41561-025-01847-5

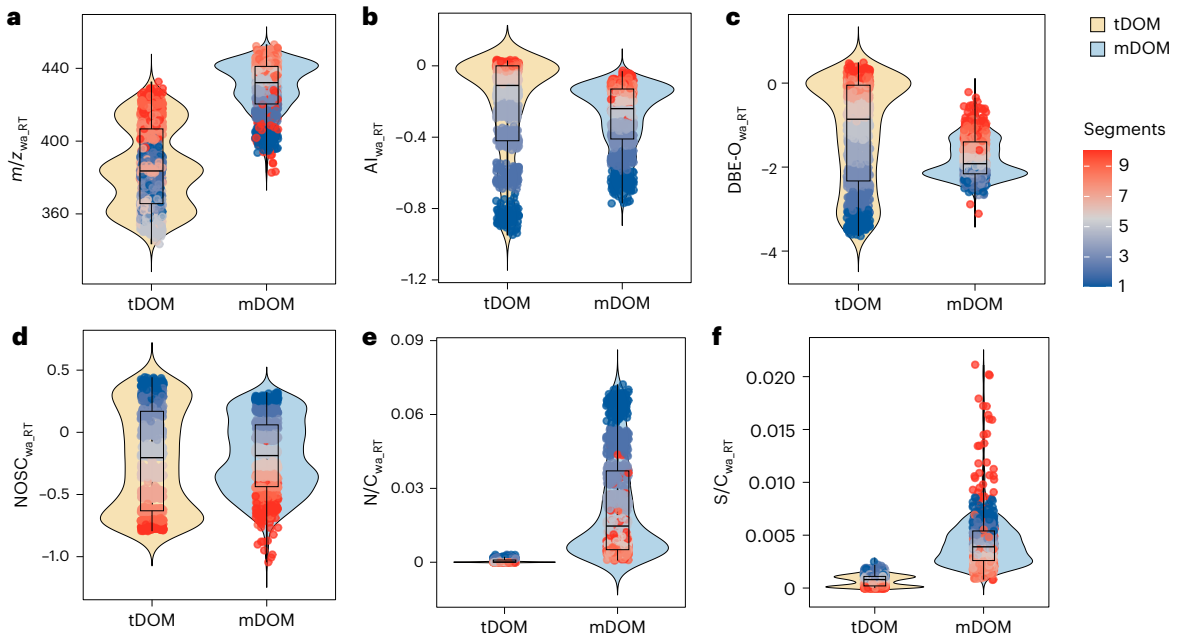

Fig. 3 | Chemical characteristics of Arctic Ocean DOM. a–f, Violin plots for intensity-weighted average (wa) LC–FTMS-derived parameters at each retention time (RT) segment (1-min interval; Methods) for water column samples ($n = 93$): m/z_{wa_RT} (**a**), AI_{wa_RT} (**b**), $DBE\text{-}O_{wa\_RT}$ (**c**), $NOSC_{wa\_RT}$ (**d**), N/C_{wa_RT} (**e**) and S/C_{wa_RT} (**f**) for tDOM (yellow) and mDOM (blue). The violin shapes represent kernel density estimates of chemical parameter distributions across retention time segments. Individual data points (MFs) are colour-coded by retention time segment. Hollow boxplots indicate the median (centre line) and interquartile range (box), and whiskers extend to the minimum and maximum values. Each violin plot is scaled to the same width for comparison. All parameters were significantly different between tDOM and mDOM at the 99% confidence level (two-sided Wilcoxon signed-rank test, $P < 0.001$).

been affected by endmember assumptions and stable carbon isotope fractionation due to oxidation processes[21]. A comparison of the tDOC quantification from our molecular-based method and the $\delta^{13}C$-based mixing model yielded a slope of 0.67 (Extended Data Fig. 3g), suggesting that our approach probably represent a lower threshold of tDOC, and the potential biases may be due to the presence of non-ionizable and high-molecular-weight compounds rather than to the choice of terrestrial proxy (Supplementary Text 3). Moreover, residuals of the DOC–TAI correlation were normally distributed (Shapiro–Wilk test, $P > 0.05$), indicating no systematic bias between terrestrial (high DOC) and marine-dominated (low DOC) samples. This supports the assumption that sample matrix effects, for example, introduced by compositional changes of non-ionizable components, do not substantially skew the DOC–TAI correlation. Despite these uncertainties, the strong correlation between tDOC concentrations derived from the $\delta^{13}C$-based mixing model and our molecule-based method (Pearson's $R^2 = 0.96$; Extended Data Fig. 3g) demonstrated a robust representation in capturing relative trends, distribution patterns and compositional variability in tDOC. However, the associated uncertainties should be considered when interpreting or applying absolute concentration values.

Chemical signatures of contrasting DOM sources

Beyond quantitative estimates, our LC–FTMS approach provided elemental and polarity information for each identified MF. Compared with marine DOM (mDOM), tDOM exhibited broader distributions of molecular weight (mass-to-charge ratio, m/z_{wa_RT}, where wa_RT represents intensity-weighted average (wa) parameters for each retention time (RT) segment in samples; Fig. 3a), aromaticity (aromaticity index, AI_{wa_RT}; Fig. 3b), unsaturation (double bond equivalent minus oxygen, $DBE\text{-}O_{wa\_RT}$; Fig. 3c) and nominal oxidation state of carbon ($NOSC_{wa\_RT}$[34]; Fig. 3d), probably reflecting progressive alteration of tDOM during turnover. This aligns with tDOC fractions of varying degradation states and ages in Arctic rivers[35]. In contrast, tDOM showed narrow ranges of low nitrogen-to-carbon (N/C_{wa_RT}) and sulfur-to-carbon (S/C_{wa_RT}) ratios (Fig. 3e,f), reflecting the typically lower nitrogen and sulfur content of plant- and soil-derived DOM compared with marine autotrophic sources[20,36]. tDOM was enriched in low-molecular-weight compounds (Fig. 3a and Extended Data Fig. 4a), probably due to rapid removal (for example, degradation, flocculation) of shelf[37,38] and permafrost-derived tDOM[39], consistent with previous findings[20]. Additionally, tDOM was dominated by less polar fractions with high AI_{wa_RT} and $DBE\text{-}O_{wa\_RT}$, but low $NOSC_{wa\_RT}$ (Fig. 3b–d and Extended Data Fig. 4b–d), reflecting a chemically mature composition typical of terrestrial sources with structurally aromatic and hydrophobic molecules[40].

Non-metric multidimensional scaling (NMDS) highlighted clear depth-dependent gradients in tDOM composition (Fig. 4a). Salinity had a strong influence on NMDS ordination (envfit's $P < 0.01$, $R^2 = 0.75$; Supplementary Table 1), but collinearity with other factors limited the interpretability of individual contributions (Fig. 4c). Partial Mantel tests, controlling the salinity effect, identified temperature, nutrients (nitrate, phosphate, silicate), DOC/dissolved organic nitrogen (DON) ratio and the fluorescence index (FI)[41] as key drivers of variability ($P < 0.05$; Fig. 4d and Supplementary Table 2). Redundancy analysis (RDA; Fig. 4b and Supplementary Table 3) attributed 29.9% of the variance to temperature (11.9%) and nutrients (15.3%), with the first axis capturing 76% of variance along the depth gradient. This underscores the role of vertical hydrography in structuring the tDOC pool, with temperature and nutrient patterns reflecting water mass origin rather than biological processing, consistent with previous findings distinguishing polar and Atlantic waters using nutrient signatures[42]. Microbial influence appeared to be limited (2.7% variance via DOC/DON and FI), supported by (1) low N/C ratio in tDOM (Fig. 3e and Extended Data Fig. 4e), consistent with the known low nitrogen signature of terrestrial-derived DOM[20]; (2) nitrate depletion in surface waters (Extended Data Fig. 5), probably due to shelf denitrification[43] and stratification limiting nutrient resupply[44]; and (3) elevated aromaticity, unsaturation and NOSC[34] in surface tDOM

https://doi.org/10.1038/s41561-025-01847-5

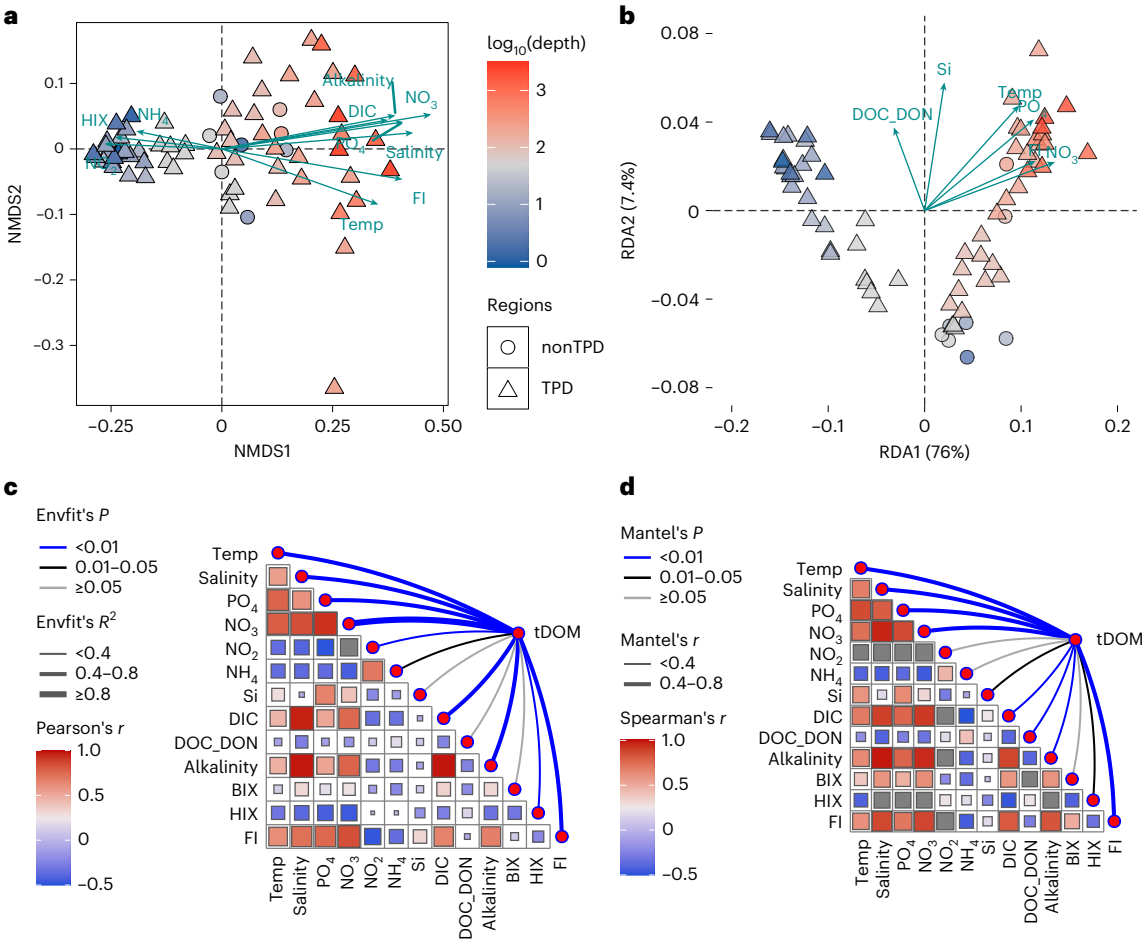

Fig. 4 | Compositional variations of tDOM. a, The dissimilarity of tDOM composition between seawater samples ($n = 70$) based on NMDS using Bray–Curtis distance. Only environmental variables that were significant at $P < 0.05$ (in green arrows) were plotted using the envfit function (DIC, dissolved inorganic carbon; temp, temperature; DOC_DON, molar DOC/DON ratio). **b**, RDA revealed variations in tDOM composition in relation to environmental parameters (in green arrows; symbols and colours as in **a**). The percentage of variation explained by each axis is shown in parentheses (for details see Supplementary Table 3). **c**, The envfit's R^2 and P values are indicated by the colour and width of the connecting lines (for details see Supplementary Table 1). Pearson's correlation coefficients between environmental parameters are shown by the colour and size of the squares. **d**, Partial Mantel tests were performed to assess the relationships between tDOM composition and environmental parameters while controlling for the effect of salinity. The corresponding r and P values are illustrated by the colour and width of the connecting lines (for details see Supplementary Table 2) and Spearman's rank correlation coefficients between environmental parameters are represented by the colour and size of squares. In **a** and **b**, symbols denote: samples inside the TPD (that is, Amundsen Basin and western Fram Strait; triangles) and outside the TPD (nonTPD; that is, western Nansen Basin and Yermak Plateau; circles). Colours in panels **a** and **b** represent $\log_{10}$-transformed water depth in metres ($\log_{10}$(depth)). Full variable names for abbreviations in figures are provided in Supplementary Tables 1–3.

(Extended Data Fig. 4b–d). These suggest thermodynamically favourable but underutilized terrestrial compounds, potentially preserved due to limited microbial degradation.

Our method allowed measuring original seawater concentrations as low as 25 µmol DOC kg^{-1} for lead waters and detected MF features in the low femtomole range[18]. During sea ice melt, a sharp gradient of salinity forms in the uppermost layer (~1 m) of lead waters (Extended Data Fig. 6). In contrast to seawater samples, DOC in lead waters (<70 µmol kg^{-1}; Fig. 5) correlated positively with the degradation index (I_{DEG})[16], N/C_{wa}, m/z_{wa} and $NOSC_{wa}$ ($P < 0.01$), reflecting a distinct sea ice melt signature captured by LC–FTMS. In the polar fraction, lower-molecular-weight compounds were associated with elevated nitrogen content and oxidation state (Fig. 6). These trends, along with low I_{DEG}[16] in low-salinity lead waters (Fig. 5a), suggested a higher bioavailability, consistent with earlier findings that fresh, algal-derived DOM from sea ice is bioavailable[45]. A related fluorescence-based study showed elevated microbial-derived DOM in low-salinity lead waters[32]. Future studies integrating polarity-resolved MF data with incubation experiments could lead to a more precise understanding of tDOM reactivity. The non-polar fraction exhibited inverse molecular trends (Fig. 6), aligning with earlier findings showing that labile DOM from sea ice melt is rapidly transformed by heterotrophic bacteria into more persistent forms[46]. The polarity-resolved approach thus offers detailed insight into the molecular characteristics of sea ice melt DOM entering the ocean.

Implications for the Arctic organic carbon cycle

Our study is based on a full-year CAO dataset and contributes a depth-resolved estimate of the tDOC inventory in the CAO. We calculated a total inventory for the CAO (volume of ca. 9.8×10^6 km^3) of 5.93 ± 0.09 PgC for DOC, of which at least 0.97 ± 0.05 PgC is tDOC (see Methods and Supplementary Table 5). For comparison, using the global ocean DOC inventory (662 PgC)[47] and the total ocean volume (1.33×10^9 km^3)[48], the DOC inventory based on the CAO volume would be 4.88 PgC. The difference between our measured total inventory and this value is ~1.05 PgC, closely aligning with our molecular-based estimate

https://doi.org/10.1038/s41561-025-01847-5

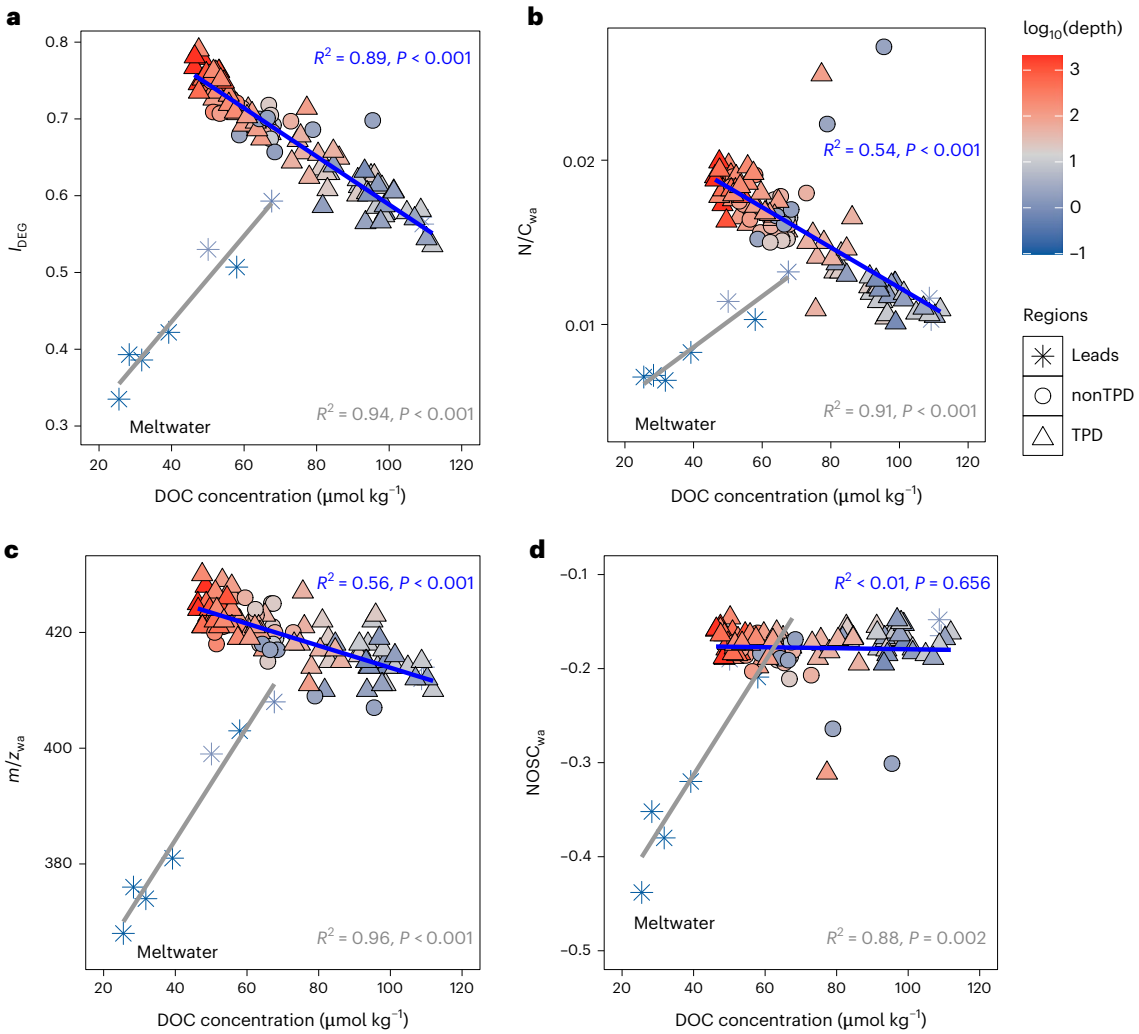

Fig. 5 | Molecular distinction of DOM from sea ice melt in lead waters. a–d, The relationship between DOC concentration and the I_{DEG} (**a**), N/C_{wa} (**b**), m/z_{wa} (**c**) and $NOSC_{wa}$ (**d**) for all Arctic samples (n = 118). Symbols represent sample groups: surface water from leads in the Amundsen Basin (asterisks), samples inside the TPD (that is, Amundsen Basin and western Fram Strait; triangles) and outside the TPD (nonTPD; that is, western Nansen Basin and Yermak Plateau; circles). Colours represent log$_{10}$-transformed water depth in metres (log$_{10}$(depth)). The blue and grey lines indicate the linear regression for seawater samples (n = 109) and low DOC concentration (<70 μmol kg^{-1}) lead water samples (n = 7), respectively. Two-sided Pearson correlation P values are shown without adjustment for multiple comparisons.

for the CAO tDOC inventory. Note that this tDOC estimate only considers the excess of Arctic Ocean DOC compared with the global average. Given the uncertainties inherent in global inventory estimates and regional variability, further validation through region-specific modelling and long-term datasets is warranted. We assume that our LC–FTMS estimate may represent a lower bound, as independent $\delta^{13}C$-based mixing models yielded a higher tDOC inventory (2.17 ± 0.07 PgC; Extended Data Fig. 3g) and higher tDOC contribution was reported for the deep Canada Basin[33]. A recent study highlights the importance of including terrestrial inputs in Earth system models, as they contribute to coastal CO_2 outgassing and reduce the Arctic Ocean carbon sink by at least 10% (33 TgC yr^{-1})[13]. Our molecular approach enables long-term tracking of tDOC concentrations and characteristics (for example, polarity, aromaticity, oxidation state, size), offering key parameters into models to improve the representation and parameterization of tDOC in future climate projections.

DOC and tDOC inventories declined sharply with depth (Fig. 2h), but tDOC still contributed substantially to the deep DOC pool (15.0% at ≥1,000 m; Supplementary Table 5). Overall, tDOC accounted for at least 16.4% of the total DOC in the CAO, driven by riverine runoff, coastal erosion, and potential benthic efflux from sediments and subsea permafrost[30,49]. Parts of this tDOC exits the Arctic Ocean with polar surface water and deep water[8]. Based on an average tDOC concentration of 31.5 ± 4.8 μmol l^{-1} in polar surface water and an outflow of 3.3 Sv (ref. 8; 1 Sv = 10^6 m^3 s^{-1}), the estimated tDOC outflow was estimated at 39.3 ± 6.0 TgC yr^{-1}, comparable to riverine DOC discharge into the Arctic Ocean (25–36 Tg DOC yr^{-1})[35]. In the deep, tDOM originates from down-slope shelf transport[50] and benthic sources[30,49] (Supplementary Fig. 1). Given an estimated average tDOC concentration of 7.9 ± 0.4 μmol l^{-1} and a 5.8 Sv overflow of deep water[8], the deep Arctic tDOC overflow was estimated at 17.3 ± 1.5 TgC yr^{-1}. It should be noted that these estimates were approximations that require refinement via higher spatiotemporal resolution. This would allow a more precise estimate of the tDOM that is transported across the CAO by the TPD, exits via Fram Strait[24], and joins Arctic deep water outflows across the Greenland–Scotland Ridge[8], ultimately integrating into North Atlantic Deep Water and global thermohaline circulation (Supplementary Fig. 1). Expanding our approach to trace tDOC along North Atlantic Deep Water pathways could enhance understanding of its long-term transformation and role in the global carbon cycle.

https://doi.org/10.1038/s41561-025-01847-5

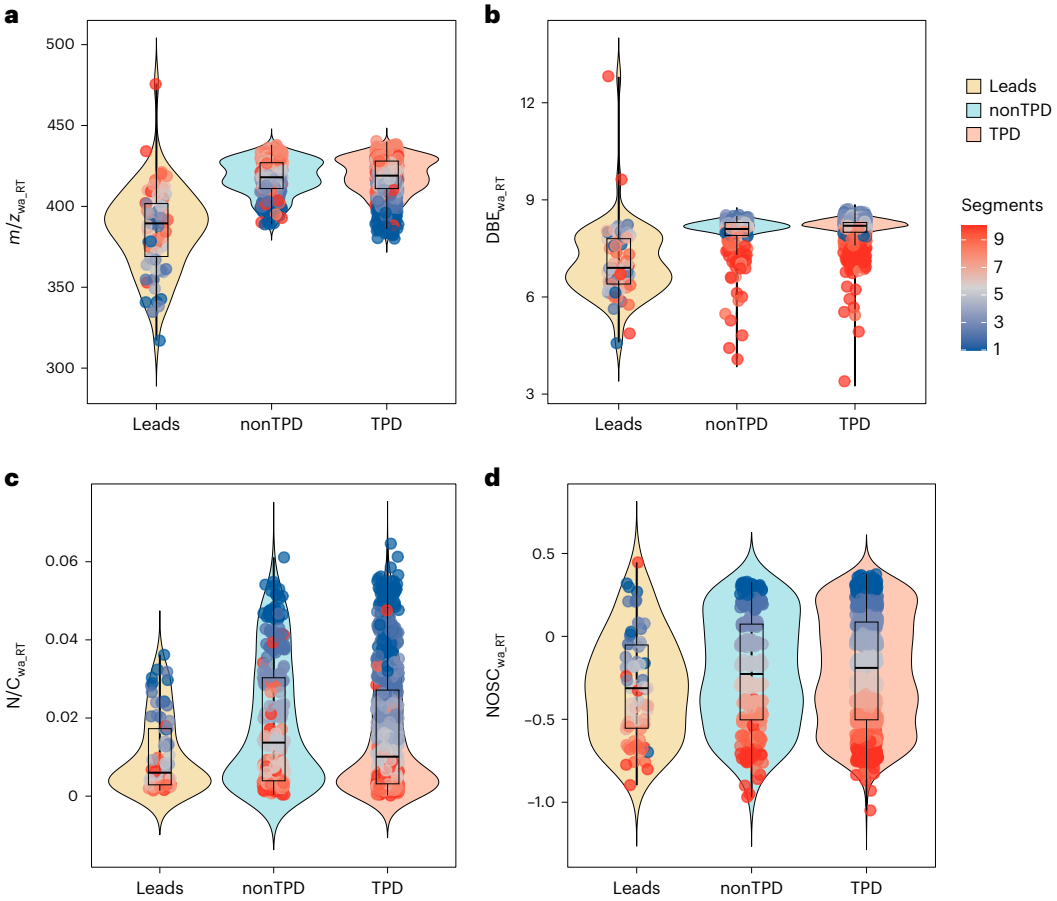

Fig. 6 | Chemical characteristics of DOM in different water types in the Arctic Ocean. a–**d**, Violin plots for distributions of intensity-weighted average LC–FTMS-derived chemical parameters in retention time (polarity) segments (1-min intervals; Methods). Higher retention times are related to lower polarity: m/z_{wa_RT} (**a**), DBE_{wa_RT} (**b**), N/C_{wa_RT} (**c**) and $NOSC_{wa\_RT}$ (**d**) for lead and ocean waters. The violin shapes represent kernel density estimates of chemical parameter distributions across retention time segments. Individual data points are colour-coded by retention time. Hollow boxplots indicate the median (centre line) and interquartile range (box), and whiskers extend to the minimum and maximum values. Each violin plot is scaled to the same width for comparison. Sample types include: lead waters with low DOC concentration (<70 µmol kg^{-1}) in the Amundsen Basin (leads; $n = 7$), samples outside the TPD (nonTPD; that is, western Nansen Basin and Yermak Plateau; $n = 27$) and samples inside the TPD (that is, Amundsen Basin and western Fram Strait; $n = 82$). Differences among sample types were evaluated using two-sided Kruskal–Wallis tests followed by two-sided post hoc Dunn's tests. All parameters differed significantly among sample types at the 95% confidence level (two-sided Kruskal–Wallis test, $P < 0.05$; Supplementary Table 4).

Online content

Any methods, additional references, Nature Portfolio reporting summaries, source data, extended data, supplementary information, acknowledgements, peer review information; details of author contributions and competing interests; and statements of data and code availability are available at https://doi.org/10.1038/s41561-025-01847-5.

References

1. Kortsch, S., Primicerio, R., Fossheim, M., Dolgov, A. V. & Aschan, M. Climate change alters the structure of Arctic marine food webs due to poleward shifts of boreal generalists. *Proc. R. Soc. B* **282**, 20151546 (2015).
2. Friedlingstein, P. et al. Global carbon budget 2023. *Earth Syst. Sci. Data* **15**, 5301–5369 (2023).
3. Yadav, J., Kumar, A. & Mohan, R. Dramatic decline of Arctic sea ice linked to global warming. *Nat. Hazards* **103**, 2617–2621 (2020).
4. Carlson, C. A. & Hansell, D. A. in *Biogeochemistry of Marine Dissolved Organic Matter* 2nd edn (eds Hansell, D. A. & Carlson, C. A.) 65–126 (Academic, 2015).
5. Charette, M. A. et al. The Transpolar Drift as a source of riverine and shelf-derived trace elements to the central Arctic Ocean. *J. Geophys. Res. Ocean.* **125**, e2019JC015920 (2020).
6. PAME *Large Marine Ecosystems (LMEs) of the Arctic Area: Revision of the Arctic LME Map 15th of May 2013: Second Edition* (PAME International Secretariat, 2013).
7. Gjelstrup, C. V. B., Myers, P. G., Lee, C. M., Azetsu-Scott, K. & Stedmon, C. A. Connectivity between Siberian river runoff and the lower limb of the Atlantic Meridional Overturning Circulation. *Limnol. Oceanogr.* **69**, 2680–2687 (2024).
8. Østerhus, S. et al. Arctic Mediterranean exchanges: a consistent volume budget and trends in transports from two decades of observations. *Ocean Sci.* **15**, 379–399 (2019).
9. Dunton, K. H., Weingartner, T. & Carmack, E. C. The nearshore western Beaufort Sea ecosystem: circulation and importance of terrestrial carbon in Arctic coastal food webs. *Prog. Oceanogr.* **71**, 362–378 (2006).
10. Hill, V. J. Impacts of chromophoric dissolved organic material on surface ocean heating in the Chukchi Sea. *J. Geophys. Res. Ocean.* **113**, C07024 (2008).
11. Roiha, T., Peura, S., Cusson, M. & Rautio, M. Allochthonous carbon is a major regulator to bacterial growth and community composition in subarctic freshwaters. *Sci. Rep.* **6**, 34456 (2016).

12. Polimene, L. et al. Biological lability of terrestrial DOM increases CO_2 outgassing across Arctic shelves. *Biogeochemistry* **160**, 289–300 (2022).
13. Oziel, L. et al. Climate change and terrigenous inputs decrease the efficiency of the future Arctic Ocean's biological carbon pump. *Nat. Clim. Change* **15**, 171–179 (2025).
14. Kong, X., Jendrossek, T., Ludwichowski, K.-U., Marx, U. & Koch, B. P. Solid-phase extraction of aquatic organic matter: loading-dependent chemical fractionation and self-assembly. *Environ. Sci. Technol.* **55**, 15495–15504 (2021).
15. Kiontke, A., Oliveira-Birkmeier, A., Opitz, A. & Birkemeyer, C. Electrospray ionization efficiency is dependent on different molecular descriptors with respect to solvent pH and instrumental configuration. *PLoS ONE* **11**, e0167502 (2016).
16. Flerus, R. et al. A molecular perspective on the ageing of marine dissolved organic matter. *Biogeosciences* **9**, 1935–1955 (2012).
17. Koch, B. P., Ludwichowski, K.-U., Kattner, G., Dittmar, T. & Witt, M. Advanced characterization of marine dissolved organic matter by combining reversed-phase liquid chromatography and FT-ICR-MS. *Mar. Chem.* **111**, 233–241 (2008).
18. Lechtenfeld, O. J., Kaesler, J., Jennings, E. K. & Koch, B. P. Direct analysis of marine dissolved organic matter using LC-FT-ICR MS. *Environ. Sci. Technol.* **58**, 4637–4647 (2024).
19. Hernes, P. J. & Benner, R. Photochemical and microbial degradation of dissolved lignin phenols: implications for the fate of terrigenous dissolved organic matter in marine environments. *J. Geophys. Res. Ocean.* **108**, 3291 (2003).
20. Amon, R. M. W. & Meon, B. The biogeochemistry of dissolved organic matter and nutrients in two large Arctic estuaries and potential implications for our understanding of the Arctic Ocean system. *Mar. Chem.* **92**, 311–330 (2004).
21. Goranov, A. I., Carter, S. J., Pearson, A. & Hatcher, P. G. Oxidation camouflages terrestrial organic matter to appear marine-like. *Environ. Sci. Technol.* **59**, 5607–5620 (2025).
22. Stedmon, C. A. & Yamashita, Y. in *Biogeochemistry of Marine Dissolved Organic Matter* 3rd edn (eds Hansell, D. A. & Carlson, C. A.) 101–136 (Academic, 2024).
23. Amon, R. M. W., Budéus, G. & Meon, B. Dissolved organic carbon distribution and origin in the Nordic seas: exchanges with the Arctic Ocean and the North Atlantic. *J. Geophys. Res. Ocean.* **108**, 3221 (2003).
24. Benner, R., Louchouarn, P. & Amon, R. M. W. Terrigenous dissolved organic matter in the Arctic Ocean and its transport to surface and deep waters of the North Atlantic. *Glob. Biogeochem. Cycles* **19**, GB2025 (2005).
25. Para, J. et al. UV/PAR radiation and DOM properties in surface coastal waters of the Canadian shelf of the Beaufort Sea during summer 2009. *Biogeosciences* **10**, 2761–2774 (2013).
26. Fong, A. A. et al. Overview of the MOSAiC expedition: ecosystem. *Elementa* **12**, 00135 (2024).
27. Coble, P. G. Marine optical biogeochemistry: the chemistry of ocean color. *Chem. Rev.* **107**, 402–418 (2007).
28. Walker, S. A., Amon, R. M. W. & Stedmon, C. A. Variations in high-latitude riverine fluorescent dissolved organic matter: a comparison of large Arctic rivers. *J. Geophys. Res. Biogeosci.* **118**, 1689–1702 (2013).
29. Chen, M., Jung, J., Lee, Y. K. & Hur, J. Surface accumulation of low molecular weight dissolved organic matter in surface waters and horizontal off-shelf spreading of nutrients and humic-like fluorescence in the Chukchi Sea of the Arctic Ocean. *Sci. Total Environ.* **639**, 624–632 (2018).
30. Chen, M. et al. Production of fluorescent dissolved organic matter in Arctic Ocean sediments. *Sci. Rep.* **6**, 39213 (2016).
31. Medeiros, P. M. et al. A novel molecular approach for tracing terrigenous dissolved organic matter into the deep ocean. *Glob. Biogeochem. Cycles* **30**, 689–699 (2016).
32. Kong, X. et al. Variability of dissolved organic matter sources in the upper Eurasian Arctic Ocean. *J. Geophys. Res. Ocean.* **129**, e2023JC020844 (2024).
33. Griffith, D. R. et al. Carbon dynamics in the western Arctic Ocean: insights from full-depth carbon isotope profiles of DIC, DOC, and POC. *Biogeosciences* **9**, 1217–1224 (2012).
34. LaRowe, D. E. & Van Cappellen, P. Degradation of natural organic matter: a thermodynamic analysis. *Geochim. Cosmochim. Acta* **75**, 2030–2042 (2011).
35. Raymond, P. A. et al. Flux and age of dissolved organic carbon exported to the Arctic Ocean: a carbon isotopic study of the five largest arctic rivers. *Glob. Biogeochem. Cycles* **21**, GB4011 (2007).
36. Seidel, M. et al. Composition and transformation of dissolved organic matter in the Baltic Sea. *Front. Earth Sci.* **5**, 31 (2017).
37. Letscher, R. T., Hansell, D. A. & Kadko, D. Rapid removal of terrigenous dissolved organic carbon over the Eurasian shelves of the Arctic Ocean. *Mar. Chem.* **123**, 78–87 (2011).
38. Sholkovitz, E. R., Boyle, E. A. & Price, N. B. The removal of dissolved humic acids and iron during estuarine mixing. *Earth Planet. Sci. Lett.* **40**, 130–136 (1978).
39. Vonk, J. E. et al. High biolability of ancient permafrost carbon upon thaw. *Geophys. Res. Lett.* **40**, 2689–2693 (2013).
40. Shi, X., Ji, L. & Zhu, D. Investigating roles of organic and inorganic soil components in sorption of polar and nonpolar aromatic compounds. *Environ. Pollut.* **158**, 319–324 (2010).
41. McKnight, D. M. et al. Spectrofluorometric characterization of dissolved organic matter for indication of precursor organic material and aromaticity. *Limnol. Oceanogr.* **46**, 38–48 (2001).
42. Ekwurzel, B., Schlosser, P., Mortlock, R. A., Fairbanks, R. G. & Swift, J. H. River runoff, sea ice meltwater, and Pacific water distribution and mean residence times in the Arctic Ocean. *J. Geophys. Res. Ocean.* **106**, 9075–9092 (2001).
43. Nitishinsky, M., Anderson, L. G. & Hölemann, J. A. Inorganic carbon and nutrient fluxes on the Arctic shelf. *Cont. Shelf Res.* **27**, 1584–1599 (2007).
44. Song, H. et al. Strong and regionally distinct links between ice-retreat timing and phytoplankton production in the Arctic Ocean. *Limnol. Oceanogr.* **66**, 2498–2508 (2021).
45. Jørgensen, L., Stedmon, C. A., Kaartokallio, H., Middelboe, M. & Thomas, D. N. Changes in the composition and bioavailability of dissolved organic matter during sea ice formation. *Limnol. Oceanogr.* **60**, 817–830 (2015).
46. Yu, J. et al. Sea ice melting drives substantial change in dissolved organic matter in surface water off Prydz Bay, east Antarctic. *J. Geophys. Res. Biogeosci.* **128**, e2023JG007415 (2023).
47. Hansell, D. A., Carlson, C. A., Repeta, D. J. & Schlitzer, R. Dissolved organic matter in the ocean: a controversy stimulates new insights. *Oceanography* **22**, 202–211 (2009).
48. Charette, M. & Smith, W. The volume of Earth's ocean. *Oceanography* **23**, 112–114 (2010).
49. Chen, M. et al. Subsea permafrost as a potential major source of dissolved organic matter to the East Siberian Arctic Shelf. *Sci. Total Environ.* **777**, 146100 (2021).
50. Wei, B. et al. Rapid down-slope transport of fresh dissolved organic matter to the deep ocean in the eastern North Atlantic. *Geophys. Res. Lett.* **51**, e2024GL110349 (2024).
51. Morison, J. et al. Changing Arctic Ocean freshwater pathways. *Nature* **481**, 66–70 (2012).
52. GEBCO Bathymetric Compilation Group 2024 *The GEBCO_2024 Grid - A Continuous Terrain Model of the Global Oceans and Land* (NERC EDS British Oceanographic Data Centre NOC, 2024); https://doi.org/10.5285/1c44ce99-0a0d-5f4f-e063-7086abc0ea0f

Methods

Sample location and collection

Seawater samples were collected from the rosette on the Central Observatory ice floe (Ocean City) and on RV *Polarstern* during the Arctic drift expedition MOSAiC (cruise PS122[26]). The drift with the sea ice floe started in the Amundsen Basin, via the western Nansen Basin and Yermak Plateau, towards the Fram Strait from November 2019 to July 2020, then the ship relocated and returned to the Amundsen Basin (near the North Pole) to drift again from August and September 2020 with a new ice floe (Fig. 1). Throughout the expedition, the ship drifted with the sea ice in the CAO, leaving the ice only near the end of the expedition. Seawater (sampling depths at approximately 2 m, 10 m, 20 m, 50 m, 100 m, 200 m, 500 m, 1,000 m, 2,000 m) was filtered through pre-combusted (450 °C, 5 h) glass fibre filters (Whatman; GF/F).

Samples from lead waters (from the surface at 0.1 m down to 1 m) were collected during the post-sea ice melt season in the Amundsen Basin during 25 August and 4 September 2019 using a peristaltic pump (Masterflex E/S portable sampler) and filtered through an inline 0.2 µm pore size cartridge filter (Sterivex; polyethersulfone membrane). The salinity of these samples was between 2.4 and 29.2 and we refer to them as 'lead water' samples. When referencing the sea ice meltwater signal derived from these samples (Fig. 5), we use the term 'sea ice meltwater endmember'.

All samples were stored in acid-washed high-density polyethylene bottles at −20 °C for DOC and LC–FTMS measurement analysis. Samples for excitation-emission matrices (FDOM EEMs) measurements were stored in pre-combusted amber glass vials at 4 °C[32]. Salinity profiles for seawater samples were acquired with a conductivity, temperature and depth (CTD) sensor attached to a rosette system. Salinity for lead water samples was measured with a hand-held multimeter (Cond 340i, WTW).

DOC and TDN measurement and determination of DOC/DON ratio

DOC and total dissolved nitrogen (TDN) was determined by high-temperature catalytic oxidation using a TOC-VCPN (Shimadzu)[53]. Water samples were directly poured into well-rinsed vials and placed in the autosampler. In the autosampler, the sample was acidified (0.1 mol l^{-1} HCl suprapur, Merck) and sparged with oxygen for 5 min to remove inorganic carbon. A sample volume of 50 µl was injected directly on the catalyst (680 °C). Detection of the generated CO_2 was performed with a non-dispersive infrared detector, with a limit of determination of 7 µmol DOC kg^{-1} and a precision of ±5%. TDN was quantified by a chemiluminescence detector, with a limit of determination of 3 µmol TDN kg^{-1} and a precision of ±7%. The DOC and DON concentrations were used to calculate the DOC/DON ratio. DON was calculated by subtracting the summed concentrations of ammonium, nitrate and nitrite from TDN. The MOSAiC nutrient data were acquired from the PANGAEA data repository[54,55].

$\delta^{13}C$ analysis

For $\delta^{13}C$ analysis of solid-phase extracted DOM, samples were acidified to pH 2 with 12 M HCl and an aliquot of 15 µgC was extracted using solid-phase extraction cartridges (PPL, 50 mg, Agilent) and eluted with methanol (HPLC grade, Merck). Extracts were filled into liquid tight tin cups and the solvent was evaporated using nitrogen (N5.0 grade). The extracts were analysed with a continuous flow isotope ratio mass spectrometer (Thermo Scientific, Delta V Plus), interfaced with an elemental analyser (Flash EA 2000 Series) connected via a ConFlo IV interface (Thermo Scientific). The isotopic ratios were expressed as parts per thousand (‰) in the δ notation[56]:

$$\delta_x = [(R_{\text{sample}}/R_{\text{standard}}) - 1] \times 1,000$$

where x represents the heavy carbon isotope ^{13}C. R_{sample} represents the $^{13}C/^{12}C$ isotope ratio relative to the corresponding standard (R_{standard}). The verification of accuracy and precision[57] was based on the secondary reference material USGS40 ($\delta^{13}C$ = −26.39‰), USGS41 ($\delta^{13}C$ = +37.63‰) and CH6 ($\delta^{13}C$ = −10.45‰), provided by Reston Stable Isotope Laboratory (RSIL) and the International Atomic Energy Agency (IAEA, Vienna). The measurement errors were <0.2‰ for stable carbon measurements. Furthermore, the laboratory standards isoleucine ($\delta^{13}C$ = −3.1‰) and acetanilide ($\delta^{13}C$ = −27.26‰) were analysed every ten samples at an accuracy of $\delta^{13}C < \pm 0.1$‰. The samples were analysed in duplicates and true δ values obtained after two-point linear normalization[58]. We used a $\delta^{13}C$ binary mixing model to assess the relative contributions of terrestrial (f_{ter}) and marine fractions (f_{mar}) to DOC:

$$\delta^{13}C_{\text{ter}} f_{\text{ter}} + \delta^{13}C_{\text{mar}} f_{\text{mar}} = \delta^{13}C_{\text{sample}}$$

$$f_{\text{ter}} + f_{\text{mar}} = 1$$

where $\delta^{13}C_{\text{sample}}$ is the $\delta^{13}C$ value of the sample. It is further required that $f_{\text{ter}} + f_{\text{mar}} = 1$, which ensures that the mass balance equation is followed. For the terrestrial and marine endmember, we used $\delta^{13}C_{\text{ter}}$ = −30‰ and $\delta^{13}C_{\text{mar}}$ = −22‰ (refs. 21,31), respectively.

Optical spectroscopy for original seawater

FDOM EEMs were measured using a spectrofluorometer (Aqualog, Horiba) equipped with a charge-coupled device detector. Excitation wavelengths were scanned from 240 to 600 nm at 3 nm increments, while collecting emission spectra from 220 to 620 nm (~3.3 nm increments). EEMs were processed by the drEEM (v0.6.3) toolbox in MATLAB (MathWorks)[59]. The fluorescence spectra were blank corrected using ultrapure water (Whatman, Milli-Q), inner filter effect correction and Raman normalization by dividing by the Raman peak of ultrapure water at an integrated excitation of 350 nm by the emission between 371 and 428 nm (Raman units)[60]. The total fluorescence intensity ($FDOM_{\text{sum}}$) was calculated as the sum of all fluorescence in each EEM spectra. The FI was calculated, based on the ratio of the emission intensity at a wavelength of 450 nm and that at 500 nm, obtained for a fixed excitation wavelength of 370 nm[41]. FI is commonly used as an indicator to identify the relative contribution of microbial and terrestrial sources to the DOM pool: lower FI values indicate a dominance of terrestrially derived substances, while higher values suggest a stronger microbial origin[61,62]. The humification index (relative degree of humification) was calculated based on the ratio of the area under the emission spectra at 435–480 nm to that at 300–345 nm with an excitation wavelength of 254 nm[63]. The biological index (proxy for freshly produced autochthonous DOM) was calculated as the ratio of the emission intensity at 380 nm divided by that at 430 nm, with a fixed excitation wavelength of 310 nm (ref. 64). Higher biological index values reflect a greater contribution of freshly produced DOM.

We applied a parallel factor (PARAFAC) analysis[59,65] for all MOSAiC FDOM samples (n = 414) to decompose EEMs into different underlying fluorescent components (Extended Data Fig. 1). Based on fluorescence maxima, C340 and C320 are typically attributed to protein-like FDOM[66,67]. C475 and C415 are generally regarded as humic-like components with terrestrial characteristics[66,68,69]. In this study, C475 was selected as a terrestrial proxy.

LC–FTMS analysis of DOM in bulk seawater

Samples were analysed in random order by LC–FTMS using a recent method[18]. For analytical quality control, we performed regular measurements of a Suwannee River fulvic acid standard (SRFA, 2S101H, International Humic Substances Society; total number of analyses in the set: n = 10) and of a pooled sample that was mixed from aliquots of ten random Arctic samples (n = 16). In each analysis, retention times <13.3 min were not recorded due to the influence of the salt matrix and data >23.3 min were removed due to the lack of DOM signatures and presence of typical solvent contaminants. The dataset was divided into ten retention time segments (1-min intervals) between 13.3 min

and 23.3 min (grey bars; Supplementary Fig. 2) and numbered from 1 to 10. Each retention time segment was internally recalibrated with a list of peaks commonly present in DOM (150–1,000 m/z), and the root mean square error was determined with ±0.4 ppm after calibration. The retention time segment separation and calibration were performed in Compass Data Analysis 5.1 software (Bruker Daltonik GmbH). Mass peak lists were generated based on a signal-to-noise ratio of $S/N \geq 4$. Using the open-access software UltraMassExplorer (UME)[70], MFs were assigned to peaks in the mass range of m/z 200–700 with elemental ranges of $C_{1-\infty}H_{1-\infty}O_{0-\infty}N_{0-2}S_{0-1}$ within a mass error of ±0.5 ppm. Additional filters were applied to the assigned MFs: $0.3 \leq H/C \leq 3.0$, $0 \leq O/C \leq 1.2$, $0 \leq N/C \leq 1.3$ and $H/C \leq 2\,C + 2 + N$[71]. The DBE and DBE-O was used to further filter the dataset having: $0 < DBE < 25$, $-10 < DBE\text{-}O < 10$ (ref. 72). All MFs present in surfactants[73] or intense MFs in blank samples were removed from the respective retention time segments. Isotopologue formulas (^{13}C) were used to verify the parent formulas for quality control but removed from the final dataset. The molecular assignments and filters were performed using R version 4.1.2 software (https://www.r-project.org/). We calculated the TAI for the entire sample run[74] (TAI, sum of intensity of all peaks having a formula assignment) and for each individual retention time segment (TAI_{RT}).

MF-based indices were calculated, such as the AI[75], NOSC[34] and I_{DEG}[16]. Intensity-weighted average parameters for each sample were abbreviated as $NOSC_{wa}$, AI_{wa}, DBE_{wa}, $DBE\text{-}O_{wa}$, H/C_{wa}, O/C_{wa}, N/C_{wa}, S/C_{wa} and m/z_{wa}. Intensity-weighted average parameters for each retention time segment in samples were abbreviated as $NOSC_{wa\_RT}$, AI_{wa_RT}, DBE_{wa_RT}, $DBE\text{-}O_{wa\_RT}$, H/C_{wa_RT}, O/C_{wa_RT}, N/C_{wa_RT}, S/C_{wa_RT} and m/z_{wa_RT}. The molecular assignments, index and ratio calculations and filtering were performed using R version 4.1.2 via UME[70].

I_{Terr} estimates the relative proportion of terrigenous material[31]. A total of 40 MFs from the pool of 184 t-Peaks (indicators of riverine input) with the highest negative correlation with $\delta^{13}C$ values (as terrestrial sources: Terr) and 40 MFs from the 'island of stability'[76] with the highest positive correlation with $\delta^{13}C$ values (as marine sources: Mar) were selected. Higher I_{Terr} values indicate a higher contribution of terrigenous material in the sample[31].

Calculations and uncertainties of tDOC concentration and inventory

To categorize the MFs, we summed the peak magnitudes of identical MFs across retention time segments of the chromatographic run. Summed MF magnitudes were normalized by the DOC concentration in each sample before performing Spearman's rank correlations with the terrigenous proxy C475. Significant correlations ($P < 0.01$, $R > 0$) were identified using R version 4.1.2 and the corrplot package. MFs positively correlated with C475 ($n = 1{,}457$) were classified as tMFs, representing 8.7% of the total number of MFs and 27.7% of total intensity (Supplementary Fig. 3b). MFs that were negatively correlated ($n = 2{,}220$) or uncorrelated ($n = 13{,}033$) were categorized as mMFs, comprising 13.3% and 78.0% of the total number of MFs, respectively, and 42.6% and 29.7% of the total intensity. These results define three DOM subfractions: tDOM, negatively correlated mDOM (mDOM_neg) and non-correlated mDOM (mDOM_non), with the last two combined into a broader mDOM category. Notably, this mDOM category does not exclusively represent marine-derived DOM but rather the remaining DOM fraction after excluding tDOM. The relative proportion and DOC concentration of each subfraction was calculated as:

$$\%_{\text{subfraction}} = \frac{CI_{\text{subfraction}}}{\sum CI_{\text{subfraction}}} \times 100$$

$$DOC_{\text{subfraction}} = \frac{DOC \times \%_{\text{subfraction}}}{100}$$

where carbon intensity (CI) for each MF was calculated by multiplying the carbon number with the respective magnitude (summed intensity). Relative proportions of each subfraction ($\%_{subfraction}$) were calculated by the CI of each subfraction, divided by the summed CI of each sample. Based on the strong linear correlation between TAI and DOC concentrations, we estimated the DOC concentration for tDOC and mDOC by multiplying the DOC concentration with the proportion of each subfraction.

The average chromatographic peak width of a MF across all samples was 3.8 min, broader than the 0.5–1 min peak width for spiked model compounds in SRFA controls. Peaks broader than 2-min retention time therefore must represent different isomers, that is, molecules with the same formula but different structures. DOC showed a significant correlation with salinity (Extended Data Fig. 6), consistent with conservative mixing behaviour previously observed in the Arctic Ocean[77,78]. Because C475 was linearly correlated with DOC (Pearson's $R^2 = 0.87$ and $P < 0.001$) and salinity (Pearson's $R^2 = 0.78$ and $P < 0.001$), it behaved conservatively in the ocean as well. Accordingly, the proportion of tMFs followed the same pattern (Extended Data Fig. 3a). The linear correlation between the total DOC concentration and the tDOC fraction (Extended Data Fig. 3a) resulted in a y-intercept of 0.612% at a DOC concentration of zero. We hypothesize that this is caused by overlapping isomers and MFs that simultaneously occur in tDOM and mDOM. By subtracting the y-intercept from the tDOC estimate and adding it to the mDOC, we refined our estimate of tDOC in deep waters to 16.3% of the total DOC. The same approach was applied to FDOM and showed that terrestrial FDOM accounted for about 4.6% of the DOC in deep water (Extended Data Fig. 3b). This correction was applied consistently in tDOC concentration estimates based on the LC–FTMS method throughout the study.

We also considered the impact of the arbitrary P value threshold on the tDOC calculation. For this, a sensitivity analysis was conducted using $P < 0.05$ and $R > 0$ for tMF identification and tDOC calculations, which resulted in 1,642 tMFs. The relative root mean square error (rRMSE) between the tDOC values at $P < 0.01$ and $R > 0$ (as applied above), and those at $P < 0.05$ and $R > 0$, was 10%. However, when correcting the bias in tDOC estimates using the zero-DOC intercept, the rRMSE between these two calculations dropped to just 3% (Extended Data Fig. 3d). This suggested that while the choice of P value affects the number of identified tMFs, it has a minimal effect on the tDOC concentration calculations.

The propagation of error (ε, expressed as coefficient of variation, CV) in the calculations of tDOC was assessed using standard error propagation methods. The uncertainties in the percentage subfraction for tDOC and TAI were estimated based on the repeated analysis ($n = 16$) of a pooled sample (mix of aliquots of ten different samples), yielding uncertainties of ±3.5% and ±11.0%, respectively. These incorporated the uncertainties in the percentage subfraction for tDOC ($\varepsilon_{\%tDOC} = \pm 3.5\%$), the DOC concentration ($\varepsilon_{DOC} = \pm 5\%$) and TAI values ($\varepsilon_{TAI} = \pm 11.0\%$). Additionally, the rRMSE from the regression between DOC and TAI ($\varepsilon_{DOC\_TAI} = \pm 13.2\%$; Fig. 2c) was included in the error propagation to obtain the uncertainty for the tDOC concentration. The propagated uncertainty for tDOC (ε_{tDOC}) was computed using the following formula:

$$\varepsilon_{tDOC} = \sqrt{(\varepsilon_{\%\,tDOC})^2 + (\varepsilon_{DOC})^2 + (\varepsilon_{TAI})^2 + (\varepsilon_{DOC\_TAI})^2}$$

Consequently, the propagated uncertainty for tDOC was ±18.2%.

To calculate inventories of DOC and tDOC in the CAO, bathymetry data from the GEBCO 2024 Grid[52] and DOC data from the MOSAiC expedition were used. We calculated the area and volume at various depth intervals, starting from sea level and progressing in increments of 100 m to the deepest depth within the CAO. The tDOC concentrations for all MOSAiC samples ($n = 313$, data not shown) were derived using a regression established between tDOC and DOC concentrations by LC–FTMS samples ($n = 93$; Extended Data Fig. 3c). Average DOC and tDOC concentrations were computed for each 100 m depth interval and multiplied by the corresponding volume to derive the DOC and tDOC

inventories (Fig. 2h). In cases where DOC data were not available for certain depth intervals, values from adjacent depth intervals were used to fill these gaps. The uncertainties in the DOC and tDOC inventories at different depth intervals were assessed by considering the propagation of error. For the DOC inventory at each depth interval, we considered the CV of the DOC concentration at each depth interval (ε_{DOC_depth}), combined with the DOC concentration uncertainty (ε_{DOC} = ±5%). The equation for the uncertainty in the DOC inventory was calculated as:

$$\varepsilon_{DOC\_inventory} = \sqrt{(\varepsilon_{DOC\_depth})^2 + (\varepsilon_{DOC})^2}$$

For the tDOC inventory at each depth interval, the CV of the tDOC concentration at each depth interval (ε_{tDOC_depth}) was considered, along with the uncertainties for DOC concentration (ε_{DOC} = ±5%) and tDOC (ε_{tDOC} =±18.2%). Additionally, the rRMSE from the regression between tDOC and DOC (ε_{tDOC_DOC} = ±5.6%; Extended Data Fig. 3c) was included in the error propagation to obtain the final uncertainty for the tDOC inventory. The equation for the uncertainty in the tDOC inventory is given by:

$$\varepsilon_{tDOC\_inventory} = \sqrt{(\varepsilon_{tDOC\_depth})^2 + (\varepsilon_{tDOC\_DOC})^2 + (\varepsilon_{tDOC})^2 + (\varepsilon_{DOC})^2}$$

Statistical analyses

Statistical analyses were performed in R studio version 4.4.3. To visualize the dissimilarity of the tDOM assemblages of seawater samples, NMDS was conducted using Bray–Curtis dissimilarity (R vegan package; metaMDS function). Environmental variables were fitted to the NMDS ordination (vegan, envfit function), with multivariate correlations assessed via 999 permutations. Only environmental variables that were significant at $P < 0.05$ were plotted on the NMDS. Mantel tests were conducted to evaluate the influence of environmental factors on tDOM assemblages, and also partial Mantel tests were conducted to exclude the effect of salinity. Mantel tests, partial Mantel tests and Pearson's or Spearman's rank correlations among environmental variables were performed (R linkET package; version 0.0.7.4). RDA was used to assess variation in tDOM composition explained by environmental parameters with 999 permutations (R vegan package). For statistical analyses, environmental variables were *z*-score normalized. Polarity-associated MF data were normalized and Hellinger-transformed to give less weight to rare formulas[79]. To test the differences of intensity-weighted average parameters for each retention time segment among different sample types (Fig. 6), Kruskal–Wallis tests followed by post hoc Dunn's tests were performed. *P* values were adjusted using the Benjamini–Hochberg correction[80].

Data availability

CTD data on the Central Observatory ice floe and on RV *Polarstern* during the MOSAiC expedition are available from the PANGAEA data repository[81–84]. DOM data for MOSAiC are archived in PANGAEA[85]. Dissolved nutrient data for MOSAiC were acquired from PANGAEA[54,55]. Dissolved inorganic carbon and total alkalinity for MOSAiC were acquired from PANGAEA[86]. The bathymetry data of the Arctic Ocean are from the GEBCO 2024 Grid (https://www.gebco.net/)[52]. The full dataset is available via Figshare at https://doi.org/10.6084/m9.figshare.29210642 (ref. 87). Source data are provided with this paper.

Code availability

LC–FTMS data were analysed using the open-access software UltraMassExplorer[70], and code for the process is publicly available via GitLab (https://gitlab.awi.de/bkoch/ume).

References

53. Ksionzek, K. B. et al. Stoichiometry, polarity, and organometallics in solid-phase extracted dissolved organic matter of the Elbe–Weser estuary. *PLoS ONE* **13**, e0203260 (2018).
54. Torres-Valdés, S. et al. Dissolved nutrients data from the PS122 MOSAiC expedition carried out onboard *Polarstern* during legs 1 to 3 [dataset]. *PANGAEA* https://doi.org/10.1594/PANGAEA.966213 (2024).
55. Torres-Valdés, S. et al. Dissolved nutrients data from the PS122 MOSAiC expedition carried out at the AWI Nutrient Facility [dataset]. *PANGAEA* https://doi.org/10.1594/PANGAEA.966217 (2024).
56. Coplen, T. B. Guidelines and recommended terms for expression of stable-isotope-ratio and gas-ratio measurement results. *Rapid Commun. Mass Spectrom.* **25**, 2538–2560 (2011).
57. Brand, W. A., Coplen, T. B., Vogl, J., Rosner, M. & Prohaska, T. Assessment of international reference materials for isotope-ratio analysis (IUPAC Technical Report). *Pure Appl. Chem.* **86**, 425–467 (2014).
58. Paul, D., Skrzypek, G. & Fórizs, I. Normalization of measured stable isotopic compositions to isotope reference scales – a review. *Rapid Commun. Mass Spectrom.* **21**, 3006–3014 (2007).
59. Murphy, K. R., Stedmon, C. A., Graeber, D. & Bro, R. Fluorescence spectroscopy and multi-way techniques. PARAFAC. *Anal. Methods* **5**, 6557–6566 (2013).
60. Lawaetz, A. J. & Stedmon, C. A. Fluorescence intensity calibration using the Raman scatter peak of water. *Appl. Spectrosc.* **63**, 936–940 (2009).
61. Johnson, M. S., Couto, E. G., Abdo, M. & Lehmann, J. Fluorescence index as an indicator of dissolved organic carbon quality in hydrologic flowpaths of forested tropical watersheds. *Biogeochemistry* **105**, 149–157 (2011).
62. Murphy, K. R. et al. Photochemistry illuminates ubiquitous organic matter fluorescence spectra. *Environ. Sci. Technol.* **52**, 11243–11250 (2018).
63. Ohno, T. Fluorescence inner-filtering correction for determining the humification index of dissolved organic matter. *Environ. Sci. Technol.* **36**, 742–746 (2002).
64. Huguet, A. et al. Properties of fluorescent dissolved organic matter in the Gironde estuary. *Org. Geochem.* **40**, 706–719 (2009).
65. Stedmon, C. A., Markager, S. & Bro, R. Tracing dissolved organic matter in aquatic environments using a new approach to fluorescence spectroscopy. *Mar. Chem.* **82**, 239–254 (2003).
66. Coble, P. G. Characterization of marine and terrestrial DOM in seawater using excitation-emission matrix spectroscopy. *Mar. Chem.* **51**, 325–346 (1996).
67. Grunert, B. K., Tzortziou, M., Neale, P., Menendez, A. & Hernes, P. DOM degradation by light and microbes along the Yukon River–coastal ocean continuum. *Sci. Rep.* **11**, 10236 (2021).
68. Gonçalves-Araujo, R. et al. Using fluorescent dissolved organic matter to trace and distinguish the origin of Arctic surface waters. *Sci. Rep.* **6**, 33978 (2016).
69. Gonçalves-Araujo, R. et al. From fresh to marine waters: characterization and fate of dissolved organic matter in the Lena River delta region, Siberia. *Front. Mar. Sci.* **2**, 108 (2015).
70. Leefmann, T., Frickenhaus, S. & Koch, B. P. UltraMassExplorer: a browser-based application for the evaluation of high-resolution mass spectrometric data. *Rapid Commun. Mass Spectrom.* **33**, 193–202 (2019).
71. Koch, B. P., Dittmar, T., Witt, M. & Kattner, G. Fundamentals of molecular formula assignment to ultrahigh resolution mass data of natural organic matter. *Anal. Chem.* **79**, 1758–1763 (2007).
72. Herzsprung, P. et al. Understanding molecular formula assignment of Fourier transform ion cyclotron resonance mass spectrometry data of natural organic matter from a chemical point of view. *Anal. Bioanal. Chem.* **406**, 7977–7987 (2014).
73. Lechtenfeld, O. J. et al. The influence of salinity on the molecular and optical properties of surface microlayers in a karstic estuary. *Mar. Chem.* **150**, 25–38 (2013).

74. Patriarca, C. et al. Character and environmental lability of cyanobacteria-derived dissolved organic matter. *Limnol. Oceanogr.* **66**, 496–509 (2021).
75. Koch, B. P. & Dittmar, T. From mass to structure: an aromaticity index for high-resolution mass data of natural organic matter. *Rapid Commun. Mass Spectrom.* **20**, 926–932 (2016).
76. Lechtenfeld, O. J. et al. Molecular transformation and degradation of refractory dissolved organic matter in the Atlantic and Southern Ocean. *Geochim. Cosmochim. Acta* **126**, 321–337 (2014).
77. Tanaka, K. et al. The conservative behavior of dissolved organic carbon in surface waters of the southern Chukchi Sea, Arctic Ocean, during early summer. *Sci. Rep.* **6**, 34123 (2016).
78. Dittmar, T. & Kattner, G. The biogeochemistry of the river and shelf ecosystem of the Arctic Ocean: a review. *Mar. Chem.* **83**, 103–120 (2003).
79. Ramette, A. Multivariate analyses in microbial ecology. *FEMS Microbiol. Ecol.* **62**, 142–160 (2007).
80. Benjamini, Y. & Hochberg, Y. Controlling the false discovery rate: a practical and powerful approach to multiple testing. *J. R. Stat. Soc. B* **57**, 289–300 (1995).
81. Tippenhauer, S. et al. Physical oceanography based on ship CTD during *Polarstern* cruise PS122 [dataset]. *PANGAEA* https://doi.org/10.1594/PANGAEA.959963 (2023).
82. Tippenhauer, S. et al. Physical oceanography based on Ocean City CTD during *Polarstern* cruise PS122 [dataset]. *PANGAEA* https://doi.org/10.1594/PANGAEA.959964 (2023).
83. Tippenhauer, S. et al. Physical oceanography water bottle samples based on ship CTD during *Polarstern* cruise PS122 [dataset]. *PANGAEA* https://doi.org/10.1594/PANGAEA.959965 (2023).
84. Tippenhauer, S. et al. Physical oceanography water bottle samples based on Ocean City CTD during *Polarstern* cruise PS122 [dataset]. *PANGAEA* https://doi.org/10.1594/PANGAEA.959966 (2023).
85. Kong, X. et al. The composition of chromophoric dissolved organic matter in central Arctic surface waters during the MOSAiC expedition [dataset bundled publication]. *PANGAEA* https://doi.org/10.1594/PANGAEA.948019 (2022).
86. Ulfsbo, A. et al. Dissolved inorganic carbon and total alkalinity of seawater samples during RV *Polarstern* expedition PS122 – MOSAiC [dataset]. *PANGAEA* https://doi.org/10.1594/PANGAEA.954969 (2023).
87. Kong, X. et al. Major terrestrial contribution to the dissolved organic carbon budget in the Arctic Ocean. *Figshare* https://doi.org/10.6084/m9.figshare.29210642 (2025).
88. Nixdorf, U. et al. MOSAiC extended acknowledgement. *Zenodo* https://doi.org/10.5281/zenodo.5541624 (2021).

Acknowledgements

We acknowledge support by the Open Access publication fund of Alfred-Wegener-Institut Helmholtz-Zentrum für Polar- und Meeresforschung. We thank all colleagues involved in the expedition of the research vessel *Polarstern* during MOSAiC in 2019–2020 (AWI_PS122_00)[88]. We are thankful to C. Burau and F. Schmidt for supporting the DOC analysis, M. De Albuquerque Woll for support in stable carbon isotope analyses, and J. P. Balmonte, E. Chamberlain, J. M. Creamean, U. Dietrich, E. Droste, L. Eggers, A. A. Fong, J. Gardner, J. Grosse, C. J. M. Hoppe, O. Müller, L. M. Olsen, S. Torres-Valdes, A. Ulfsbo and L. Heitmann for collecting DOM samples during MOSAiC.

Author contributions

X.K., O.J.L., J.M.K. and B.P.K. performed the LC–FTMS experiments, and designed and improved the instrumentation. X.K. and B.P.K. designed the study and analysed the LC–FTMS data. X.K. and M.A.G. performed stable carbon isotope measurements. X.K. carried out FDOM analyses and data evaluation, with support by C.A.S. and M.A.G. X.K. wrote the manuscript. All authors contributed to the discussion and the final version of the manuscript.

Funding

Open access funding provided by Alfred-Wegener-Institut Helmholtz-Zentrum für Polar- und Meeresforschung (AWI).

Competing interests

The authors declare no competing interests.

Additional information

Extended data is available for this paper at https://doi.org/10.1038/s41561-025-01847-5.

Supplementary information The online version contains supplementary material available at https://doi.org/10.1038/s41561-025-01847-5.

Correspondence and requests for materials should be addressed to Xianyu Kong or Boris P. Koch.

Peer review information *Nature Geoscience* thanks Meilian Chen and the other, anonymous, reviewer(s) for their contribution to the peer review of this work. Primary Handling Editor: James Super, in collaboration with the *Nature Geoscience* team.

https://doi.org/10.1038/s41561-025-01847-5

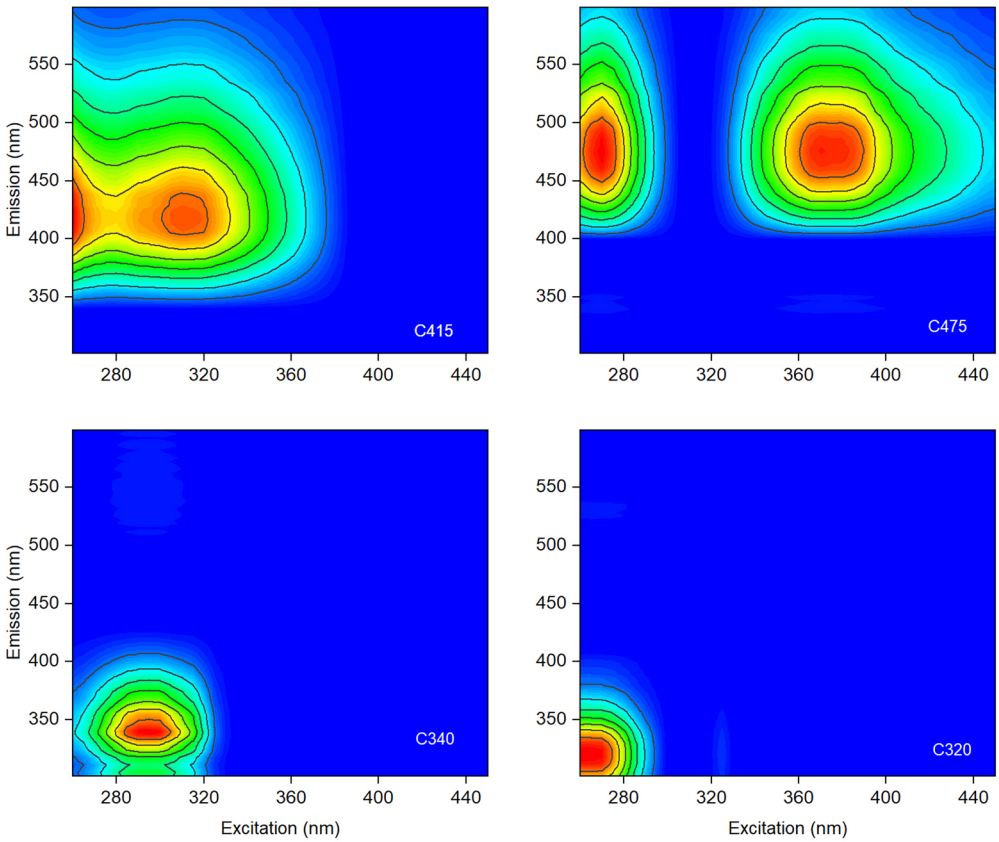

Extended Data Fig. 1 | Contour plots of the four-component PARAFAC model. Model developed from fluorescence excitation-emission matrices (EEMs) recorded for ocean and lead samples.

https://doi.org/10.1038/s41561-025-01847-5

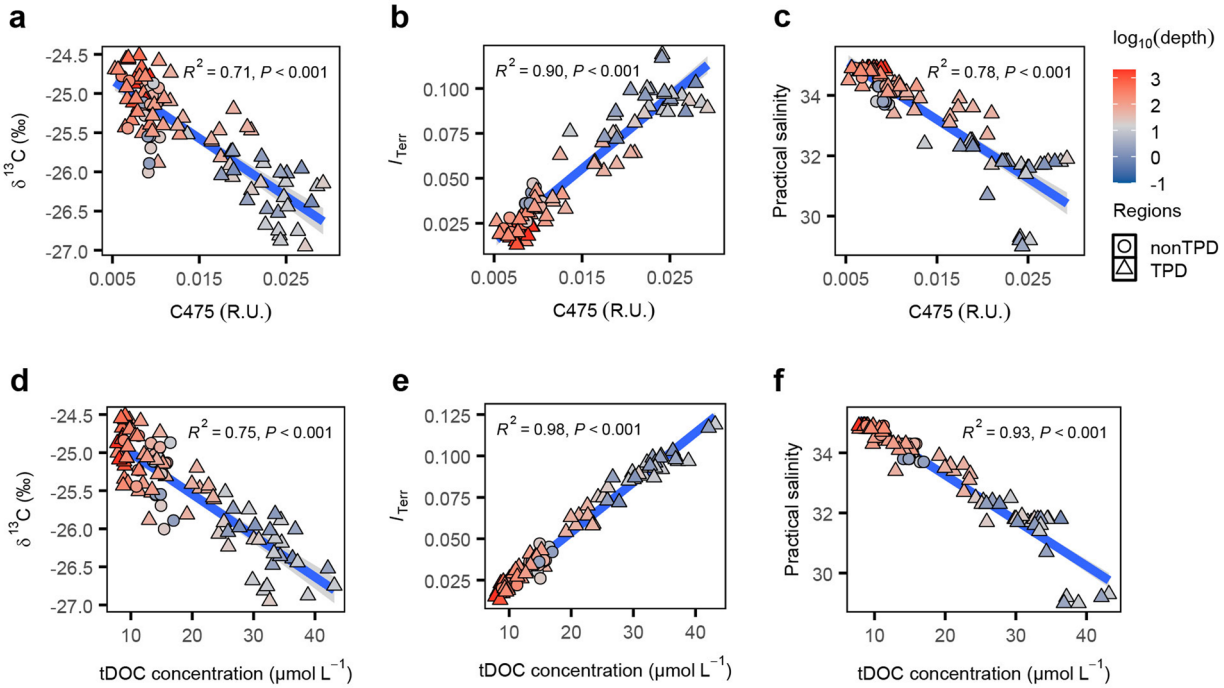

Extended Data Fig. 2 | Validation of terrestrial dissolved organic carbon (tDOC) quantification. The relationship between (**a**) stable carbon isotope $\delta^{13}C$ and C475, (**b**) terrestrial proxy I_{Terr} and C475, (**c**) practical salinity and C475, (**d**) $\delta^{13}C$ and tDOC concentration, (**e**) I_{Terr} and tDOC concentration, and (**f**) practical salinity and tDOC concentration for water column samples (n = 93). Two-sided Pearson correlation *P* values are shown in panels **a**–**f** without adjustment for multiple comparisons. Triangles denote seawater samples inside the influence of the Transpolar Drift (TPD; that is, Amundsen Basin, and western Fram Strait); circles denote seawater samples outside the influence of TPD (nonTPD; that is, western Nansen Basin and Yermak Plateau). Colours represent $\log_{10}$-transformed water depth in meters ($\log_{10}$(depth)). The blue line indicates the Pearson regression for all samples and grey shading represents the 95% confidence interval.

https://doi.org/10.1038/s41561-025-01847-5

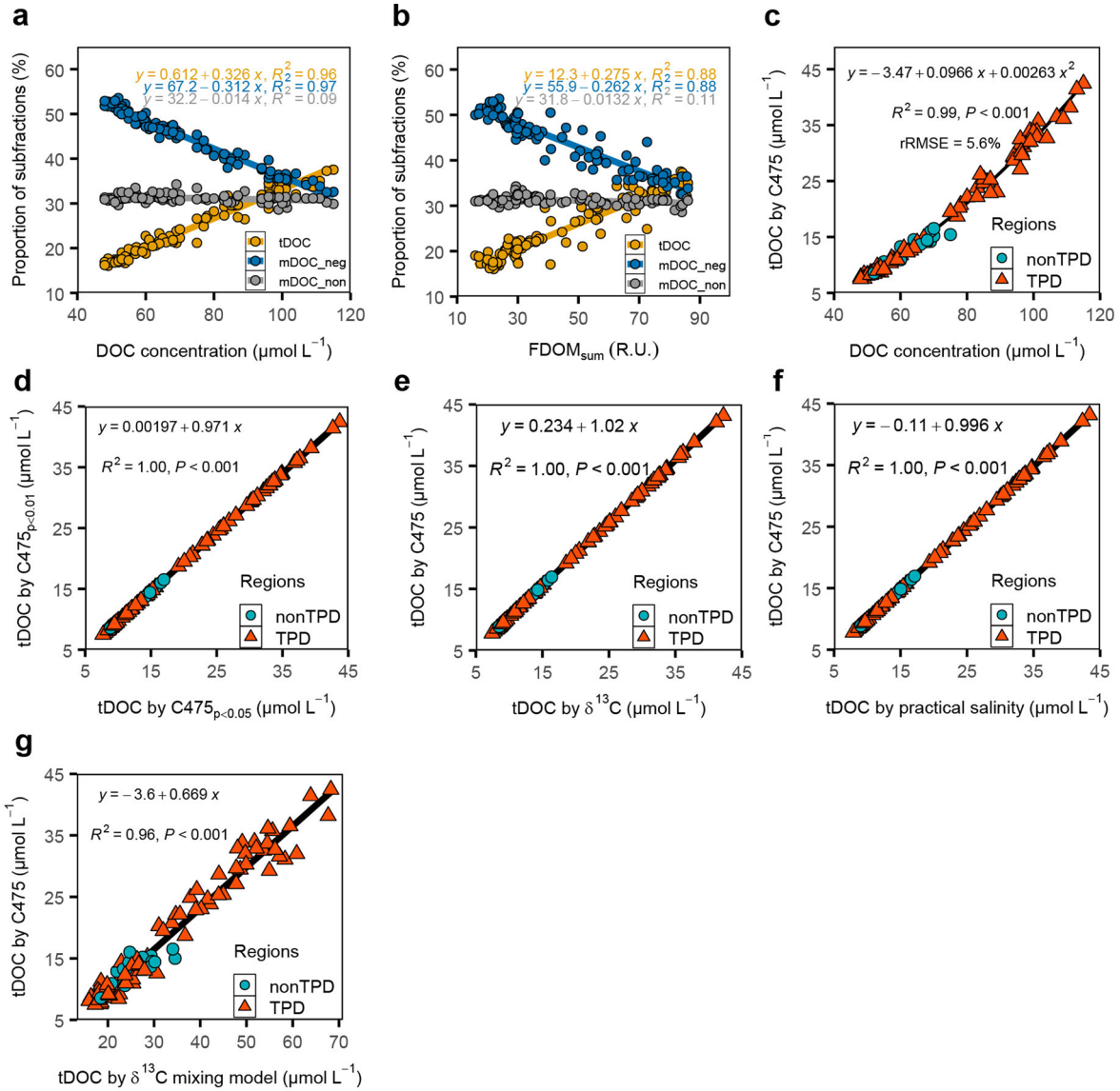

Extended Data Fig. 3 | Calibration for terrestrial dissolved organic carbon (tDOC) concentration. Correlations (n = 93) between (**a**) relative proportion of each subfraction of dissolved organic matter (DOM) and DOC concentrations, (**b**) relative proportion for each subfraction of DOM and $FDOM_{sum}$, (**c**) tDOC concentration identified by C475 (two-sided Spearman's rank $P < 0.01$) and DOC concentration (quadratic regression, two-sided F-test: $P < 0.001$), (**d**) tDOC identified by C475 (two-sided Spearman's rank $P < 0.01$) and tDOC identified by C475 (two-sided Spearman's rank $P < 0.05$), (**e**) tDOC identified by C475 and tDOC identified by $\delta^{13}C$, (**f**) tDOC identified by C475 and tDOC identified by practical salinity, (**g**) tDOC identified by C475 and tDOC identified by $\delta^{13}C$ binary mixing model for water column samples. Two-sided Pearson correlation *P* values are shown in panels **d**–**g** without adjustment for multiple comparisons. Triangles denote seawater samples inside the influence of the Transpolar Drift (TPD; that is, Amundsen Basin, and western Fram Strait); circles denote seawater samples outside the TPD influence (nonTPD; that is, western Nansen Basin and Yermak Plateau).

https://doi.org/10.1038/s41561-025-01847-5

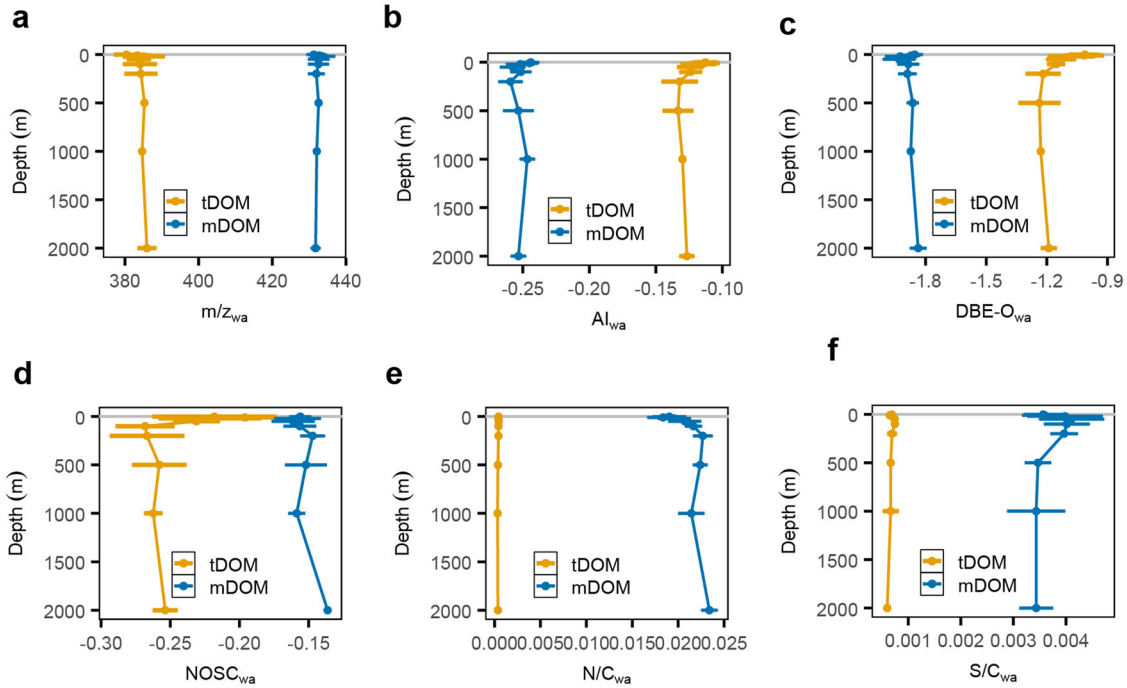

Extended Data Fig. 4 | Chemical characteristics of dissolved organic matter (DOM) subfractions in the Arctic. Distribution of intensity-weighted average (wa) LC-FTMS-derived chemical parameters for terrestrial DOM (tDOM) and marine DOM (mDOM) in water column samples (n = 93): (**a**) mass to charge ratio (m/z_{wa}), (**b**) aromaticity index (AI_{wa}), (**c**) double bond equivalent minus oxygen ($DBE\text{-}O_{wa}$), (**d**) nominal oxidation state of carbon ($NOSC_{wa}$), (**e**) nitrogen to carbon ratio (N/C_{wa}), and (**f**) sulphur to carbon ratio (S/C_{wa}). Data are presented as mean ± SD. All parameters were significantly different between tDOM and mDOM at the 99% confidence level (two-sided Wilcoxon signed-rank test, $P < 0.001$).

https://doi.org/10.1038/s41561-025-01847-5

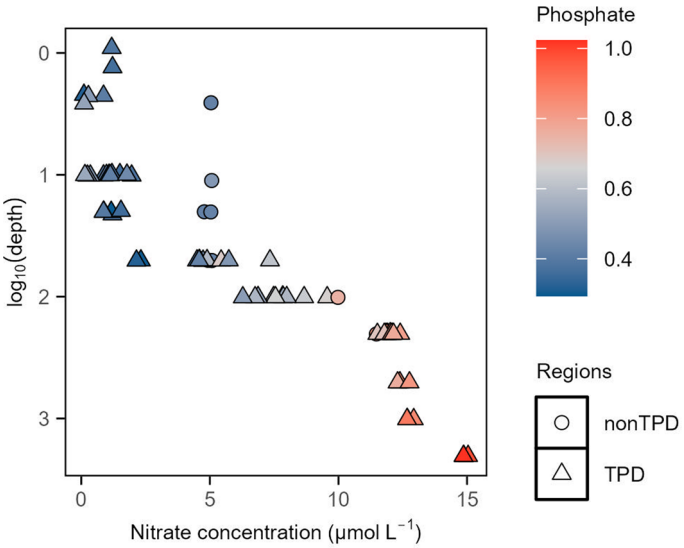

Extended Data Fig. 5 | The nitrate concentrations with depth in the Arctic Ocean (n = 70). Triangles denote seawater samples inside the influence of the Transpolar Drift (TPD; that is, Amundsen Basin, and western Fram Strait); circles denote seawater samples outside the influence of TPD (nonTPD; that is, western Nansen Basin and Yermak Plateau). The y-axis represents $\log_{10}$-transformed water depth in meters ($\log_{10}$(depth)). Colours represent phosphate concentrations in µmol L^{-1}.

https://doi.org/10.1038/s41561-025-01847-5

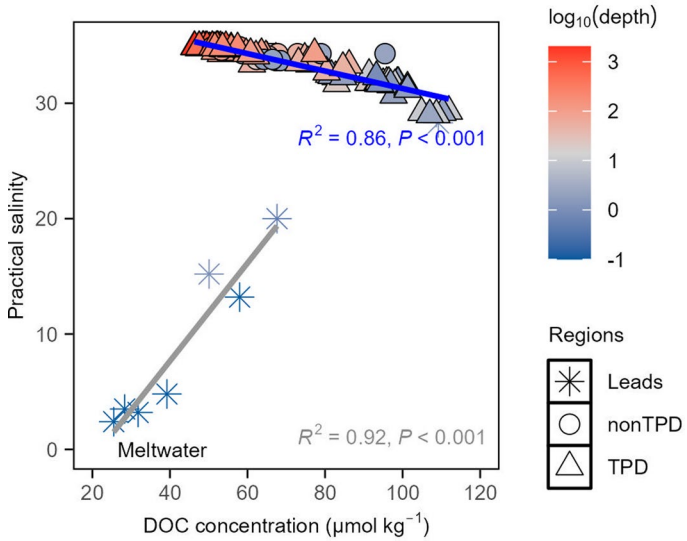

Extended Data Fig. 6 | The relationship between practical salinity and dissolved organic carbon (DOC) concentration for ocean and lead samples (n = 118). Asterisks denote surface water samples from leads in the Amundsen Basin; triangles denote seawater samples inside the influence of the Transpolar Drift (TPD; that is, Amundsen Basin, and western Fram Strait); circles denote seawater samples outside the influence of TPD (nonTPD; that is, western Nansen Basin and Yermak Plateau). Colours represent $\log_{10}$-transformed water depth in meters ($\log_{10}$(depth)). The blue line indicates the linear regression for seawater samples (n = 109). The grey line indicates the linear regression for lead water samples with low DOC concentration (< 70 µmol kg^{-1}; n = 7). Two-sided Pearson correlation *P* values are shown without adjustment for multiple comparisons.